AIAA JOURNAL
Vol. 46, No. 6, June 2008

# Effect of Energy Pulse on 3-D Edney IV Interaction

Hong Yan*
*Wright State University, Dayton, Ohio 45435*
and
Datta Gaitonde†
*U.S. Air Force Research Laboratory, Wright–Patterson AFB, Ohio 45433*

DOI: 10.2514/1.31530

**This study investigates the effect of energy deposition on pressure and thermal loads generated by an Edney IV interaction. This complex supersonic jet impingement problem is formed by the intersection of an oblique shock generated by a 15-deg wedge with a Mach 3.45 bow shock in front of a 0.0254-m diam sphere. The full three-dimensional Reynolds-averaged Navier–Stokes equations are solved with the $k$–$\omega$ turbulence model. Mesh-resolved simulations show that surface pressure without energy addition is in good agreement with experiments. The peak value is 1.8 times that observed without the impinging shock. Results from a grid resolution study confirm that the surface pressure is less sensitive than the heat flux. For flow control, a spherical energy pulse with a volume of 3 $mm^3$ and energy of 283 mJ is deposited upstream of the primary triple point. The unsteady interaction of the energy spot and its induced blast wave with the oblique shock, the distorted bow shock, and the impinging supersonic jet is elucidated in the context of the "lensing" phenomenon. The simulations indicate significant impact of the energy deposition on the surface pressure and heat flux. The instantaneous surface pressure and heat flux rise when the blast wave and high-energy spot hit the surface and fall when the expansion waves reach the surface. However, the overall integrated stress and thermal loads are reduced, mainly due to the effect of the expansion waves.**

## Nomenclature

| | | |
|---|---|---|
| $c_p$ | = | specific heat at constant pressure |
| $c_v$ | = | specific heat at constant volume |
| $D$ | = | diameter of sphere |
| $M$ | = | Mach number |
| $Pr$ | = | Prandtl number |
| $p$ | = | static pressure |
| $q$ | = | heat flux |
| $T$ | = | temperature |
| $t$ | = | time |
| $U$ | = | velocity |
| $\Delta$ | = | shock standoff distance |
| $\epsilon_Q$ | = | absorption rate |
| $\mu$ | = | dynamic viscosity |
| $\rho$ | = | density |

*Subscripts*

| | | |
|---|---|---|
| $w$ | = | value at wall |
| 0 | = | stagnation value |
| $\infty$ | = | freestream value |

## Introduction

SHOCK-ON-SHOCK interactions occurring in the vicinity of surfaces are of significant interest in the development of high-speed vehicles because of their profound impact on thermomechanical loading. For example, forebody shocks are designed to impinge on cowl lips to optimize mass capture in inlets and often lead to catastrophic failure because of the shock-on-cowl lip interactions.

When an incident oblique shock impinges on a bow shock, one of six different interference patterns is possible according to the strength of the impinging shock and the location of the intersection point relative to the bow shock. Edney [1] showed that the interference increases heating, which can result from one or more of the following mechanisms: shock/boundary-layer interaction, free shear layer attachment, and supersonic jet impingement. Of these patterns, the Edney IV interaction (Fig. 1) is one of the most striking: a supersonic jet is formed by the interaction of an incident oblique shock with a bow shock, resulting in a significant increase of heat fluxes and pressure in a concentrated region on the surface. The peak heat transfer can be several orders of magnitude higher than the ordinary stagnation heat transfer of the isolated body. Control of the formation and development of the supersonic jet can alleviate the heat transfer rate.

Several efforts by Adelgren et al. [2], Kandala and Candler [3], Kogan and Starodubtsev [4], Gaitonde and Miller [5], Trumble and Candler [6], Wieting and Holden [7], Yan and Gaitonde [8], and Zhong [9] have explored the structure and control of the Edney IV interaction by means of energy deposition and magnetogasdynamic force (MGD). Adelgren et al. [2] performed a series of experiments, in which a single laser pulse was introduced upstream of a 3-D Edney IV interaction. The experiments demonstrated the effectiveness of laser-based energy deposition in the reduction of surface pressure: the instantaneous peak value was reduced by 30% compared to the value observed without energy deposition. Kandala and Candler [3] performed a three-dimensional simulation, wherein the Navier–Stokes equations incorporated with a plasma formation model and chemical kinetics model were used to simulate a pulsed laser spot interacting with the Edney IV structures. The flow conditions were chosen to simulate the experiments performed by Adelgren et al. [2]. The peak surface pressure and heat transfer rate were reduced due to the change of shock structures caused by the interaction of the energy spot with the incident shock and blunt body shock. No quantitative comparison was made with the experiments by Adelgren et al. [2]. Kogan and Starodubtsev [4] examined the effect of a continuous heat source which was added upstream of the interaction in a 2-D flow. The results indicated that the energy addition effectively reduced the instantaneous peak pressure and heat

Presented as Paper 3344 at the 3rd AIAA Flow Control Conference, San Francisco, California, 5–8 June 2006; received 11 April 2007; revision received 30 January 2008; accepted for publication 31 January 2008. 

*Research Professor, Department of Mechanical and Materials Engineering, 3640 Colonel Glenn Highway. Senior Member AIAA.

†Techinical Area Leader, Computational Sciences Branch, Aeronautical Sciences Division, Air Vehicles Directorate. Fellow AIAA.

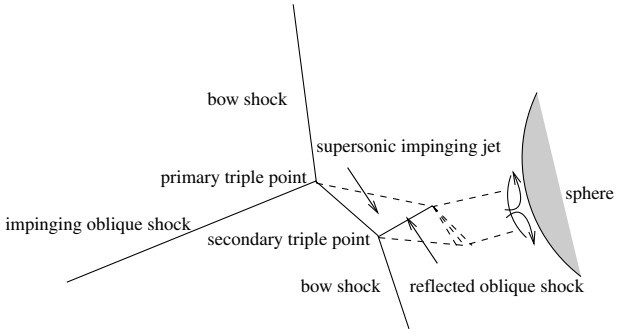


**Fig. 1 Edney IV interaction.**

fluxes with only a very small fraction of the heat resulting in an increase in the integral heat fluxes. Gaitonde and Miller [5] used electromagnetic forces to reduce heat loads on the surface by altering the structural form of the interaction and reducing the strength of the impinging supersonic jet under both electrodeless and electrode-based conditions. Trumble and Candler [6] conducted a simulation to understand the effect of laser energy deposition on an Edney IV interaction over a swept fin. The results showed that the laser energy deposition did not mitigate the localized heat flux in this configuration. Wieting and Holden [7] conducted an experimental study of two-dimensional shock-wave interference heating on a cylindrical leading edge at Mach numbers of 6.3, 6.5, and 8.0. This study provided detailed pressure and heat flux distribution. Yan and Gaitonde [8] performed a three-dimensional simulation to reproduce the experimental results by Adelgren et al. [2]. The results on a relatively coarse grid indicated that the integrated pressure load was alleviated due to the impingement of the expansion wave onto the surface. Zhong [9] conducted a two-dimensional numerical study on the Edney IV interaction at a Mach number of 8.0. The pressure and heat flux showed good agreement with the experiment by Wieting and Holden [7]. The inherent unsteadiness of the Edney IV interaction was demonstrated.

The objective of this paper is to employ high-fidelity numerical simulations to reproduce recently obtained experimental observations and to elucidate the physics of the unsteady evolution of the flowfield and surface loads due to pulsed energy deposition.

## Experimental Conditions

Experimental efforts conducted in the Rutgers University Mach 3.45 supersonic wind tunnel have been detailed by Adelgren et al. in [2]. The operating stagnation temperature and pressure are 290 K and $1.4 \times 10^6$ Pa, respectively. The Reynolds number based on the sphere diameter (0.0254 m) is $1.863 \times 10^6$. An Edney IV interaction is generated in the test section by the intersection of an oblique shock generated by a 15-deg wedge mounted on the test section ceiling. The energy spot with a focal volume of 3 m m$^3$ and energy of 283 mJ is generated by focusing a pulsed Nd:YAG laser through a 250-mm focal length lens. The Nd:YAG laser is frequency doubled to a wavelength of 532 nm with a temporal pulse width of about 10 ns and a repetition rate of 10 Hz.

## Numerical Methodology

The three-dimensional Reynolds-averaged Navier–Stokes equations are used to represent the flowfield. The flow solver GASPex is used, wherein the third-order accurate Roe scheme with Harten correction [10] along with the min-mod limiter is employed in each direction for inviscid fluxes to suppress the "carbuncle" phenomenon and central second-order differences are used for viscous terms. The fourth-order Runge–Kutta scheme is used for the time integration. The effects of fine-scale turbulence are described by the $k$–$\omega$ turbulence model [11]. The $k$–$\omega$ models predict free shear flows well. In contrast to the $k$–$\epsilon$ models, the $k$–$\omega$ models solve the laminar subregion of the turbulent boundary layer without the introduction of additional new low Reynolds number terms or the use of a wall function.

The numerical model reproduces the experiment to the extent possible. A Mach 3.45 incoming flow forms a bow shock in front of a sphere with a diameter of 0.0254 m. The Reynolds number and the freestream stagnation values are extracted from the experiment [2] as described earlier. An incident oblique shock is generated by imposing jump conditions, thus impinges onto the bow shock with a flow deflection angle of 15 deg. The Mach number behind the impinging shock is 2.57. The resulting interaction between impinging and bow shocks results in the distortion of the latter and the formation of triple points.

The energy deposition region is in the shape of a narrow band, stretched in the laser incident direction [3]. However, this hot spot is highly distorted by the impinging shock before it reaches the interaction region as presented in the following section. Meanwhile, based on our previous study [12,13], the blast wave becomes spherical 5–10 $\mu$s after the pulse. Therefore, the initial energy pulse is assumed to be a sphere in the simulation. The spherical energy pulse with the same properties as the experiments [2] is added instantaneously upstream of the primary triple point with its center located in the $z = 0$ plane, 1 sphere diameter upstream of the sphere and 0.45 diameter above the $x = 0$ plane. Because the pulse width of the laser is 10 ns, which is much smaller than the characteristic flow time scale ($D/U_\infty \approx 40$ $\mu$s), the energy deposited into the flow can be considered an instantaneous event. The inviscid perfect gas model assumes an initial Gaussian distribution for the static temperature in the spherical focal region of the laser pulse

$$T = T_i + \Delta T_o e^{-r^2/r_o^2} \tag{1}$$

where $T_i$ is the temperature at the beginning of the energy deposition. The peak temperature rise $\Delta T_o$ is related to the total energy of the laser pulse $Q_T$ by

$$\Delta T_o = \frac{\epsilon_Q Q_T}{\pi^{3/2} r_o^3 \rho_i c_v} \tag{2}$$

where $r_o$ is chosen to be one-half of the radius $R_o$ of the focal volume $V_o = \frac{4}{3}\pi R_o^3$, $c_v$ is assumed constant, and $\rho_i$ is the density at the beginning of the energy deposition. The coefficient $\epsilon_Q$ must be determined by comparison with experiment and is expected to be a function of the laser energy pulse $Q_T$ and ambient conditions in the region of the energy deposition. The initial density in the focal region is assumed to be constant at the instant of energy deposition.

At inflow boundaries, the flow vector is specified, which satisfies the Rankine–Hugoniot conditions appropriate to the impinging shock. The wall is assumed to be no slip and isothermal at $T_w = 209$ K, which is lower than the recovery temperature. By convention, positive heat flux denotes the surface heating process, while negative values indicate surface cooling. At outflow boundaries, first-order extrapolation is applied because the flow is supersonic except very near the wall.

## Comparison with Experiment

### Grid Refinement

A well-defined and refined grid is required to accurately predict the surface pressure, heat flux and details of the shear layer instabilities and shock–shock interaction structures near the surface. For ideal nonreacting gas, several studies have been performed [8] to establish resolution requirements to ensure that shear layer instability and surface loads are resolved. The structure of grid employed is shown in Fig. 2. Mesh clustering is enhanced in the region where high gradients are encountered, such as between the surface and the bow shock, and around the energy pulse.

Because no theoretical or experimental data of peak heat flux in Edney IV interactions are available, the flow past a sphere is employed to determine the grid resolution within the shock standoff distance. Van Driest's formula [14] for the heat flux at the stagnation point of a sphere is

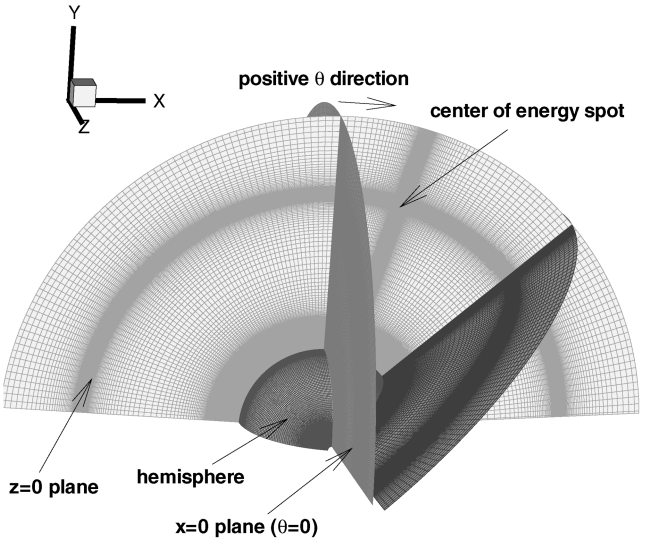


**Fig. 2 Grid configuration.**

$$q_{\text{van}} = 0.763 Pr^{-0.6} \sqrt{\rho_{02}\mu_{02}} \sqrt{\frac{2}{D}} \left[\frac{2(p_{02} - p_\infty)}{\rho_{02}}\right]^{1/4} c_p (T_{01} - T_w) \tag{3}$$

The subscripts 1 and 2 indicate the conditions before and after the normal shock, respectively, and $Pr = 0.72$. The Van Driest heat flux $q_{\text{van}}$ is $8.95 \times 10^4$ w/m$^2$ for the Mach 3.45 sphere case. For the steady-state condition, the shock standoff distance is obtained from the correlation by Billig [15],

$$\Delta = 0.0715 De^{3.24/M_\infty^2} \tag{4}$$

The peak surface pressure is the stagnation pressure behind the bow shock, which can be obtained through the Rayleigh supersonic pitot formula ($2.53 \times 10^5$ Pa). The grid resolution is measured by the number of grid points within the shock standoff distance ($\Delta$) and the ratio of the first grid spacing away from the surface and the diameter of the sphere ($\Delta r_1/D$) in the normal-wall direction. The number of grid points in the other two directions is fixed. Table 1 shows the properties of four different meshes and the comparison of the peak surface pressure and stagnation heat flux with the theoretical value. The spacing is varied by an order of magnitude. The pressure and heat flux are nondimensionalized by the stagnation pressure and the Van Driest heat flux $q_{\text{van}}$ on the surface of the sphere, respectively. The study shows that the surface pressure is less sensitive to the grid resolution than the heat flux. The former is virtually unchanged with mesh resolution, while the latter varies from extremely low values to the expected value on the finer meshes. Both grids 3 and 4 show good comparison with the Van Driest heat flux with errors restricted to 10% and 7% of the theoretical value, respectively. Based on these studies, to reduce the computational expense, resolution constraints of grid 3 are employed for the fine mesh, while the coarse grid employed in the Edney IV interaction case before for exploratory studies is similar to that in grid 1. The coarse and fine grids have a total of $6 \times 10^6$ and $17 \times 10^6$ cells, respectively. Results will focus on those obtained on the fine grid.

**Table 1 Grid refinement for a sphere**

| Grid | Grid points within $\Delta$ | $\frac{\Delta_{r1}}{D}$ | Peak surface pressure | Stagnation heat flux |
|---|---|---|---|---|
| 1 | 32 | $2.603 \times 10^{-3}$ | 0.99 | 0.040 |
| 2 | 94 | $4.850 \times 10^{-4}$ | 1.00 | 0.780 |
| 3 | 114 | $3.235 \times 10^{-4}$ | 1.00 | 0.90 |
| 4 | 154 | $1.617 \times 10^{-4}$ | 1.00 | 0.93 |

**Baseline Edney IV Interaction**

The baseline simulations are described first. In the following, the plotted temperature is normalized by the theoretical adiabatic wall temperature and pressure and density are normalized by the theoretical stagnation values behind a Mach 3.45 bow shock. Further, in all three-dimensional contour plots, the temperature and Mach number contours on the hemisphere are shown on the first grid plane away from the surface, while other variables are shown on the surface. Figure 1 displays the basic structures of the Edney IV interaction shock pattern. Two three-shock $\lambda$ patterns are observed at their corresponding triple point. The first $\lambda$ pattern is generated by the interaction of an impinging oblique shock with a bow shock. A strong vortex sheet emanates from the primary triple point. A second $\lambda$ pattern is observed at the intersection between the reflected shock and the continuation of the strong bow shock. An additional oblique wave is reflected upward at the secondary triple point and a second vortex sheet is produced. A supersonic jet embedded in the surrounding subsonic shock layer is bounded by two vortex sheets and entrains the subsonic flow into it. The jet impinges onto the sphere and is balanced by a terminating shock in front of the sphere.

Figures 3 and 4 show the pressure and temperature contours. As expected, the pressure behind the distorted bow shock is not symmetric about the $x = 0$ plane as in the isolated sphere. The pressure and temperature on each side of the jet immediately behind the distorted bow shock (zones 1 and 2) can be estimated as the values behind two normal shocks. One has the freestream Mach number of 3.45 and another has the impinging Mach number of 2.57 before the normal shock. This estimation gives pressure and temperature rise ratios of 1.8 and 1.0 cross the jet, respectively, which is consistent

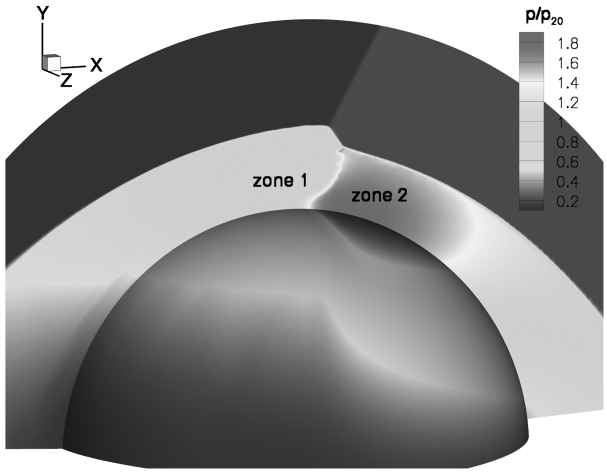


**Fig. 3 Static pressure contours.**

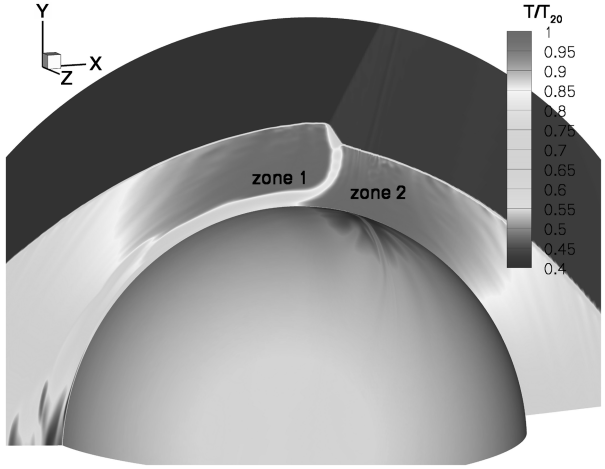


**Fig. 4 Static temperature contours.**

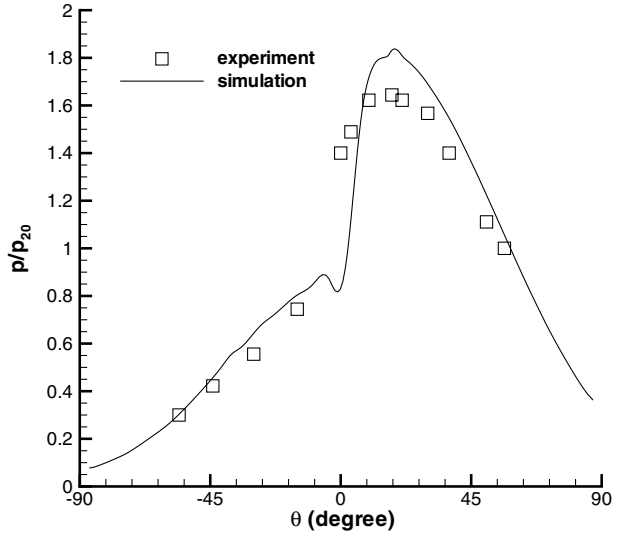


**Fig. 5 Surface pressure for baseline case.**

with the observation in Figs. 3 and 4. The stagnation pressure ratio between zone 2 and zone 1 is about 2, causing the jet to turn to the left toward the lower stagnation pressure zone (zone 1). The temperature in the impinging jet area is lower than that behind the distorted bow shock because the temperature rise is smaller through a series of oblique shocks in the jet than that cross a nearly normal shock.

Figure 5 compares the predicted surface pressure in the $z = 0$ plane to the experimental data taken from [2]. The angle $\theta$ is the polar angle in the $x - y$ plane and is measured clockwise from the $y$ axis as shown in Fig. 2. The surface pressure is in good agreement with the experiment. Relative to the flow past a sphere, the peak surface pressure is shifted to the right, where the enveloping shock becomes oblique. The peak pressure is increased to about 1.8 times as much as for flow over the sphere, because for the same flow condition before the shock, the stagnation pressure behind an oblique shock is greater than that behind a normal shock. Surface loads are generally lower than that in the 2-D simulation because of the relief effect associated with the 3-D configuration. Because of the lack of experimental data for the surface heat flux, only the numerically predicted result is presented in Fig. 6. The surface heat flux is nondimensionalized by the predicted stagnation heat flux ($0.90q_{\text{van}}$) for the sphere, which is obtained from the fine grid simulation (grid 3) shown in Table 1. Following the same trend as surface pressure, the peak surface heat flux is shifted to the right. The magnitude increases by a factor of 1.61 compared to the sphere. As indicated by Eq. (3), the increase in stagnation heat flux is correlated to the rise in stagnation pressure and density.

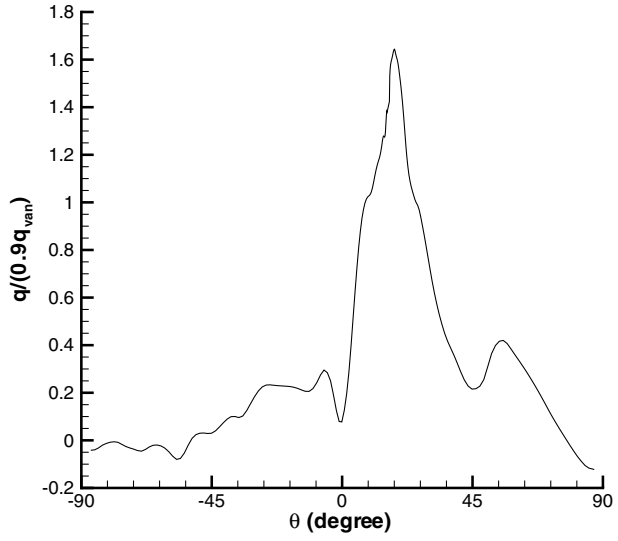


**Fig. 6 Heat flux for baseline case.**

### Edney IV Interaction with Energy Deposition

After the simulation has reached a relatively stable state, a 3-mm$^3$ spherical spot of 283 mJ is deposited in the freestream upstream of the primary triple point. In the simulation, the deposited energy is assumed to be completely absorbed by air with $\epsilon_Q = 1.0$, while in the experiment, only partial energy is absorbed by plasma and the rest is used to ionize the gas and radiated off. Although real gas effects are excited because the initial peak temperature inside the energy spot reaches as high as $1.1 \times 10^6$ K, which is obtained from the perfect gas model in Eq. (1), previous studies on the energy deposition in quiescent air [12] have shown that after the initial transient ($<10$ $\mu$s), the pressure, temperature, and velocity distributions along the radius predicted by the perfect gas model were in good agreement with experiment. In addition, this study is focused on the fluid dynamics effect of an energy pulse. Therefore, the plasma formation and chemical reactions are not considered here.

The choice of $\epsilon_Q$ is determined by matching the position of the blast wave induced by a single laser pulse in the uniform ambient condition in the simulation with the experimental data. The simulation adopts a separate numerical procedure with the assumption of a spherical laser pulse. The details are presented by Yan et al. [12]. However, in the current case, the energy spot and its induced blast wave are highly distorted by the impinging oblique shock, which makes it impossible to calibrate $\epsilon_Q$. In addition, the choice of $\epsilon_Q$ does not affect the fluid dynamics effect of an energy pulse characterized by an increase in local temperature and pressure, therefore, $\epsilon_Q$ is set to 1.

As described in [2], three major events in the energy deposition process play an important role in establishing the effect of the energy deposition on the Edney IV interaction. The first event is when the high-energy spot-induced blast wave interacts with the bow shock and the subsequent wave structures reach the surface, causing the rise in surface pressure and heat flux. The second event is when the high-energy spot interacts with the complex shock structures in the vicinity of the surface, resulting in the upstream movement of the bow shock and subsequently, the decrease in surface pressure and heat flux. The third event is when the high-energy spot hits the surface, leading to the rise in surface pressure and heat flux. Each of these experimentally observed phenomena is captured by the numerical simulation.

Figures 7 and 8 show the contours of predicted surface pressure and heat flux of the $z = 0$ plane in a $\theta$–$t$ plane, where the energy pulse is instantaneously deposited into the flowfield at $t = 0$ $\mu$s. The contours in these two figures exhibit complex flow structures

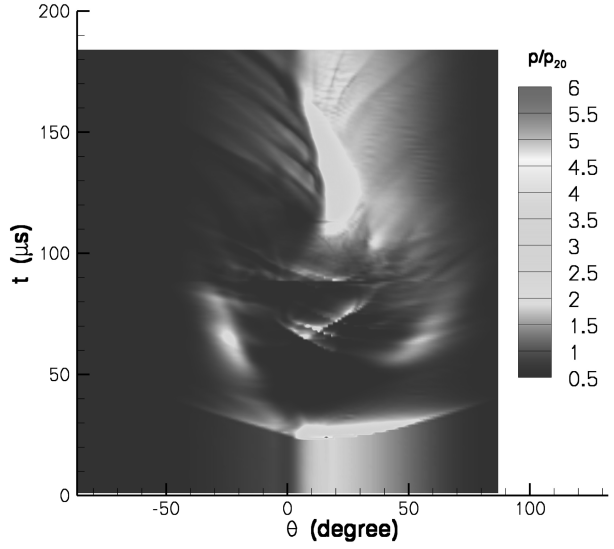


**Fig. 7 Surface pressure contours on $\theta$–$t$ plane.**

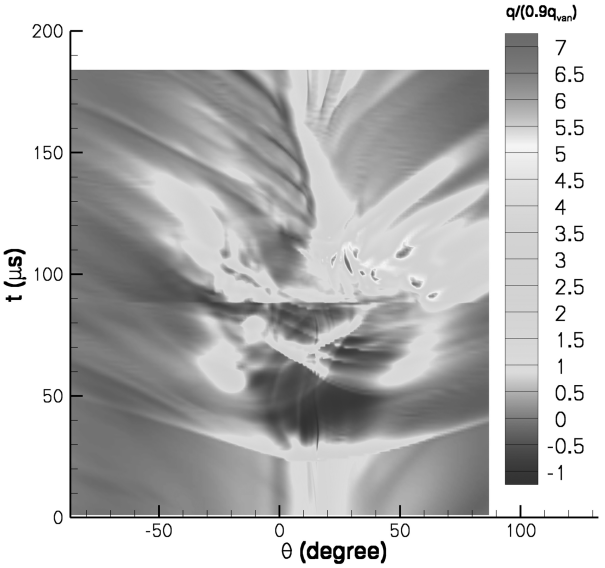


**Fig. 8 Heat flux contours on $\theta$–$t$ plane.**

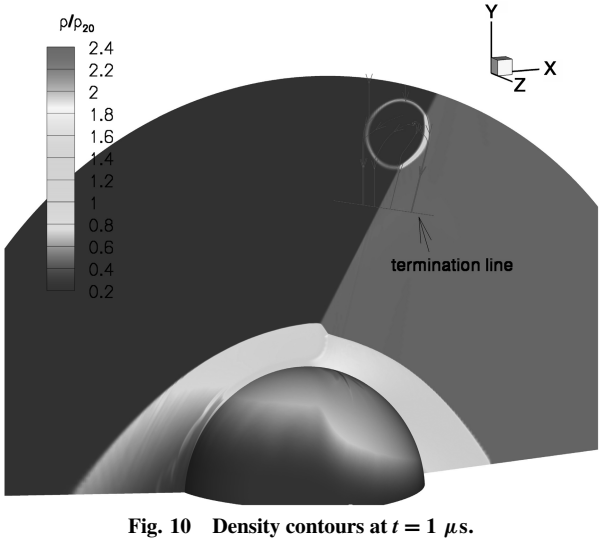


**Fig. 10 Density contours at $t = 1$ $\mu$s.**

generated by the interaction of the energy spot and expansion and blast waves with the sphere. The surface pressure and heat flux display a correlated pattern. Basically in these two figures, three distinct regions divided in the time axis are characterized by the increased ($20 < t < 30$ $\mu$s), decreased ($30 < t < 80$ $\mu$s), and increased ($80 < t < 150$ $\mu$s) surface pressure and heat flux, respectively. They correspond to the effect of the blast wave, expansion waves, and high-energy spot hitting the surface, respectively. This indicates that the effect of the high-energy spot on both surface pressure and heat flux lasts longer than that of the blast wave. It is seen that the peak surface pressure in Fig. 7 during $20 < t < 30$ $\mu$s is about 2 times that during $80 < t < 150$ $\mu$s, while the peak heat flux in Fig. 8 during $80 < t < 150$ $\mu$s is about 3 times that during $20 < t < 30$ $\mu$s. Thus the effect of the high-energy spot is much greater on heat flux than on surface pressure, while the effect of the blast wave is greater on surface pressure than on heat flux. During the time when the expansion waves hit the surface, both surface pressure and heat surface decrease, even briefly cooling portions of the surface as shown by negative heat flux in Fig. 8.

The detailed flow structure is now described to more clearly elucidate the physics of these phenomena. A series of snapshots at several time instants are shown in Figs. 9–11 to illustrate the main flow features. An energy pulse creates a low Mach number (Fig. 9) and density region (Fig. 10) in the freestream. The spot propagates radially while convecting with the local flow as clearly shown by the instantaneous streamlines in Fig. 10. The effect of an energy pulse on the flowfield in the quiescent air is characterized by a blast wave and a high-temperature core. The blast wave weakens rapidly until it propagates at the local speed of sound. As the energy spot encounters the oblique shock, it becomes elongated and stretched along the incident shock direction, causing the oblique shock to distort.

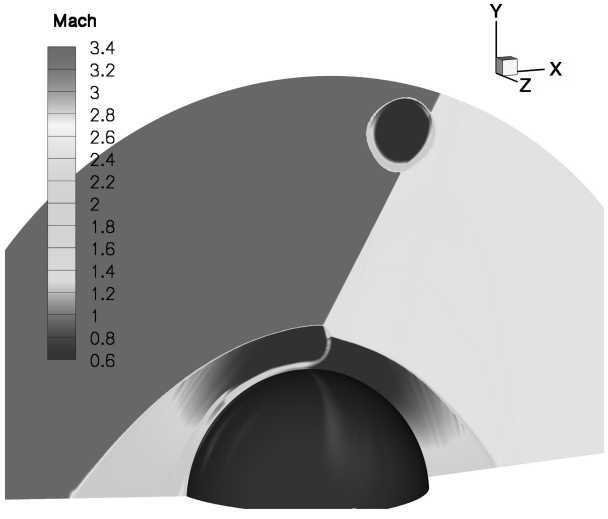


**Fig. 9 Mach number contours at $t = 1$ $\mu$s.**

Figures 11a–11e show a series of snapshots of the predicted pressure contours in the $z = 0$ plane. The experimental schlieren images are shown in Figs. 12a–12c for comparison. Once the energy is deposited, the local pressure rises rapidly due to the propagating blast wave. The pressure rise behind the oblique shock is higher than that in the freestream as shown in Fig. 11a because the local pressure behind the oblique shock is higher than that in the freestream, leading to a stronger compression of the blast wave. During $20 < t < 30$ $\mu$s, the blast wave induced by the energy spot initiates a perturbation to the Edney IV interaction location. Figure 11b demonstrates some of the main features during this time duration. The blast wave convects downstream at the local flow speed and distorts the incident shock and impinging jet. The blast wave is partly reflected off of the sphere surface and partly transmitted around the sphere. The surface pressure increases significantly when the blast wave hits the surface as shown in Fig. 11b, which is also observed in the schlieren image as a bright spot in the vicinity of the surface in Fig. 12a. By the time the blast wave transports around the sphere, the high-energy spot begins to interact with the shock structures. The interaction creates a more complex flow structure as shown in Figs. 11c and 12b at $t = 50$ $\mu$s. The bow shock moves away from the surface while the expansion waves move toward it, resulting in the reduction in surface pressure and heat flux observed in Fig. 8. Adelgren [16] described this interaction by using a one-dimensional analysis of a shock-wave interaction with a temperature discontinuity. This phenomenon is termed as the lensing effect by Georgievski and Levin [17]. Subsequently, the distorted high-energy spot along with the downstream portion of the blast wave convects onto the surface, yielding the rise in surface pressure and heat flux as shown in Fig. 11d and Fig. 8 at $t = 94$ $\mu$s. This observation is consistent with that in the experiment shown in Fig. 12c. Finally, the bow shock resumes its steady-state shape as shown in Fig. 11e. Although the solution has not yet reached the initial no-control state, the simulation does not yield any indication of hysteresis.

From the standpoint of effectiveness, in addition to localized transient peaks, integrated values of pressure (drag) and heat transfer are also of interest. Figure 13 shows the variation of the surface-integrated pressure and heat flux with time. The observed variations can be correlated to the phenomena described above. The surface pressure and heat flux show an initial increase caused by the energy pulse induced blast wave, followed by a reduction when the series of expansion waves dominate the surface interaction. When the high-energy spot together with the weakened blast wave convects toward

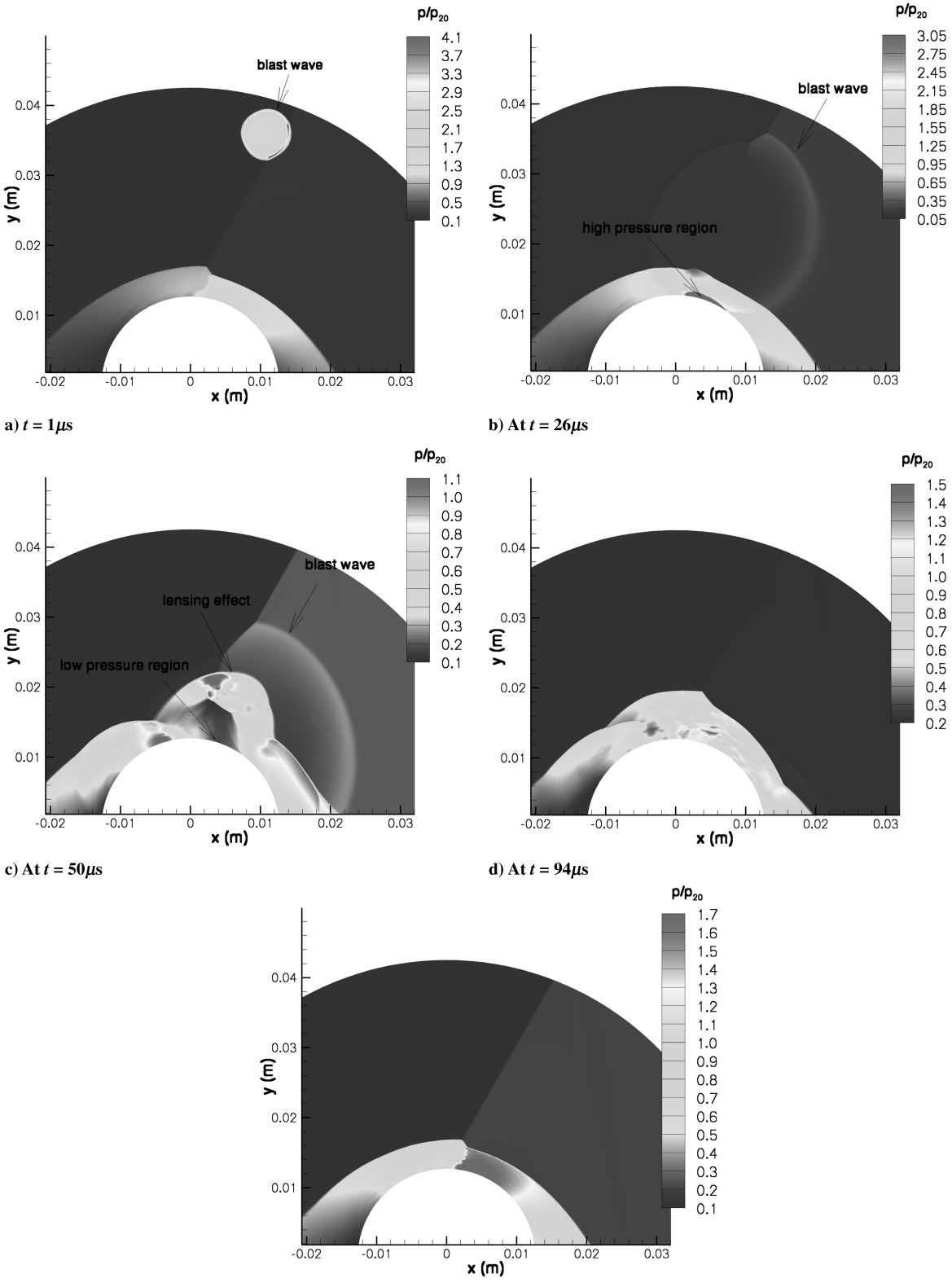


a) $t = 1\mu s$

b) At $t = 26\mu s$

c) At $t = 50\mu s$

d) At $t = 94\mu s$

e) At $t = 184\mu s$

**Fig. 11 Simulated pressure contours at different time instants.**

the surface and interacts with the distorted shock structures in the vicinity of the surface, the surface pressure and heat flux increases again. However, the second rise due to energy pulse is not large enough for the surface pressure to reach above the initial value. Overall, the pressure load is alleviated during the energy deposition process due to the effect of the expansion waves except during a very short period of time (10 $\mu$s) when the blast wave first hits the surface. For heat flux, the second rise is larger than the first. In addition, because the energy spot results in a broader gradual increase than the blast wave, the high-energy spot becomes a major contributor to the amplification of the heat flux.

Figure 14 shows the time-averaged surface pressure and heat flux in the $z = 0$ plane. Comparison with Fig. 13 suggests that the peak surface pressure and heat flux decrease from 1.8 to 1.5 and 1.6 to 1.0,

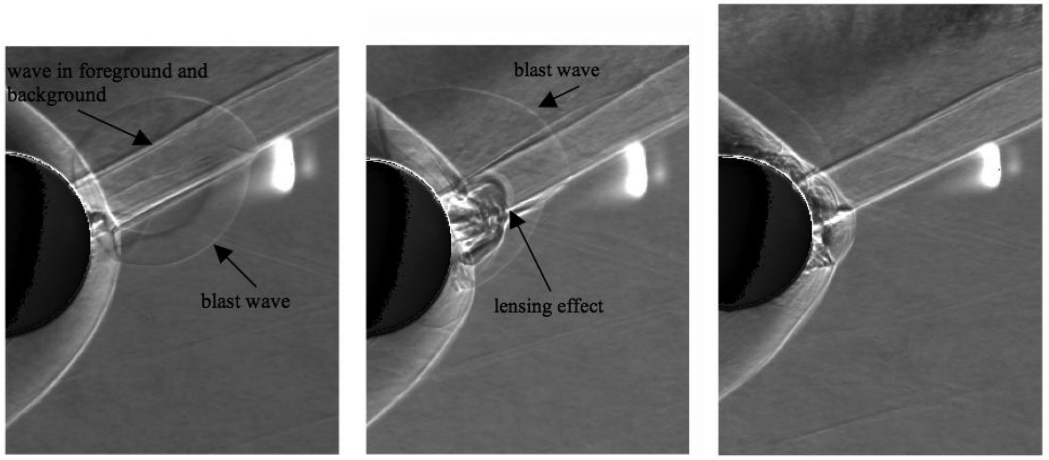


a) At $t = 30\mu s$ b) At $t = 50\mu s$ c) At $t = 90\mu s$

**Fig. 12 Schlieren images at different time instants.**

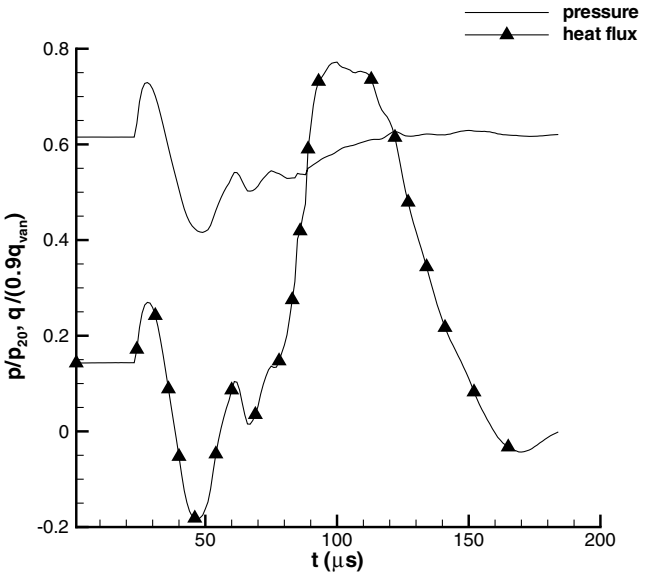


**Fig. 13 Surface-integrated pressure and heat flux versus time.**

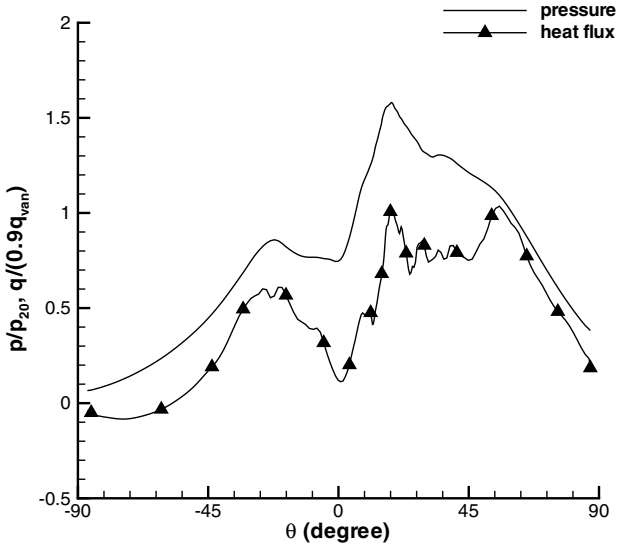


**Fig. 14 Time-averaged pressure and heat flux on $z = 0$ plane.**

about 17 and 30% compared to that without energy deposition, respectively. The surface-time-integrated surface pressure and heat flux are decreased by 11 and 4%, respectively. The total heating on the surface over a period of 184 $\mu$s is 0.25 mJ, only 0.1% of the total deposited energy. Most of the energy in the spot is effectively convected downstream as a consequence of the altered flow structures.

## Conclusions

Energy deposition is explored as a local flow control technique to achieve a transient modification to heat and pressure loads in a three-dimensional Edney IV interaction. The simulation successfully captures the main physics in the Edney IV interaction and the effect of energy deposition on this flow structure. First, the predicted surface pressure without the energy deposition is in good agreement with the experiment. Second, after the energy pulse is deposited, the instantaneous surface pressure and heat flux experience a rise, a subsequent decrease followed by a second rise in time, mainly due to the impingement of the blast wave, expansion waves, and high-energy spot onto the surface, respectively. These predictions are consistent with the experimental observation and with the lensing phenomenon. A detailed study shows that the surface-time-integrated value surface pressure and heat flux are reduced by 11 and 4%, respectively. Therefore, in the current case, the total stress and thermal load are alleviated to some extent. However, instantaneous peaks are larger and must be factored into the overall effectiveness. This study also shows that the high-energy spot impingement is the main source of surface heating, with little effect on surface pressure.

## Acknowledgments

This research is supported by the U.S. Air Force Office of Scientific Research (AFOSR) under tasks monitored by John Schmisseur and Fariba Fahroo. All simulation was performed at the National Center for Supercomputing Applications (NCSA) using a Xeon cluster. Their support is appreciated. Sincere thanks to Joseph Shang for his valuable insight on the paper.

## References

[1] Edney, B., "Anomalous Heat Transfer and Pressure Distribution on Blunt Bodies at Hypersonic Speeds in the Presence of an Impinging Shock," *The Aeronautical Research Institute of Sweden*, FAA Rept. 115, 1968.

[2] Adelgren, R., Yan, H., Elliott, G., Knight, D., Beutner, T., and Zheltovodov, A., "Control of Edney IV Interaction by Pulsed Laser Energy Deposition," *AIAA Journal*, Vol. 43, No. 2, 2005, pp. 256–269.

[3] Kandala, R., and Candler, G., "Numerical Studies of Laser-Induced Energy Deposition for Supersonic Flow Control," *AIAA Journal*, Vol. 42, No. 11, 2004, pp. 2266–2275.

[4] Kogan, M. N., and Starodubtsev, M. A., "Reduction of Peak Heat Fluxes by Supplying Heat to the Free Stream," *Fluid Dynamics*, Vol. 38, No. 1, 2003, pp. 115–125. doi:10.1023/A:1023399331201

[5] Gaitonde, D. V., and Miller, J. H., "Numerical Exploration of Shock Interaction Control with Plasma-Based Techniques," AIAA Paper 2003-3483, June 2003.

[6] Trumble, K. A., and Candler, G. V., "Flow Control of Swept Fin Shock Interactions by Laser-Induced Plasmas," AIAA Paper 2006-405, 2006.

[7] Wieting, A. R., and Holden, M., "Experimental Shock-Wave Interference Heating on a Cylinder at Mach 6 and 8," *AIAA Journal*, Vol. 27, No. 11, 1989, pp. 1557–1565.

[8] Yan, H., and Gaitonde, D., "Control of Edney IV Interaction of Energy Pulse," AIAA Paper 2006-0562, Jan. 2006.

[9] Zhong, X. L., "Application of Essentially Nonoscillatory Schemes to Unsteady Hypersonic Shock-Shock Interference Heating Problems," *AIAA Journal*, Vol. 32, No. 8, 1994, pp. 1606–1616.

[10] Roe, P., "Approximate Riemann Solvers, Parameter Vectors and Difference Schemes," *Journal of Computational Physics*, Vol. 43, No. 2, 1981, pp. 357–372. doi:10.1016/0021-9991(81)90128-5

[11] Wilcox, D. C., *Turbulence Modeling for CFD*, 2nd ed., DCW Industries, Inc., La Canada, CA, 1998, pp. 119–122.

[12] Yan, H., Adelgren, R., Boguszko, M., Elliott, G., and Knight, D., "Laser Energy Deposition in Quiescent Air," *AIAA Journal*, Vol. 41, No. 10, 2003, pp. 1988–1995.

[13] Yan, H., Knight, D., Kandala, R., and Candler, G., "Effect of a Laser Pulse on a Normal Shock," *AIAA Journal*, Vol. 45, No. 6, 2007, pp. 1270–1280. doi:10.2514/1.18283

[14] Van Driest, E. R., "The Problem of Aerodynamic Heating," *Aeronautical Engineering Review*, Vol. 15, No. 10, 1956, pp. 26–41.

[15] Billig, F. S., "Shock-Wave Shapes Around Spherical- and Cylindrical-Nosed Bodies," *Journal of Spacecraft and Rockets*, Vol. 4, No. 6, 1967, pp. 822–823.

[16] Adelgren, R., "Localized Flow Control with Energy Deposition," Ph.D. Dissertation, Department of Mechanical and Aerospace Engineering, Rutgers University, Piscataway, NJ, Sept. 2002.

[17] Georgievski, P., and Levin, V., "Unsteady Interaction of a Sphere with Atmosphere Temperature Inhomogeneity at Supersonic Speed," *Fluid Dynamics*, Vol. 28, No. 4, 1993, pp. 568–574. doi:10.1007/BF01342694

N. Clemens
*Associate Editor*